remote sensing

MDPI

Article

AM–GM Algorithm for Evaluating, Analyzing, and Correcting the Spatial Scaling Bias of the Leaf Area Index

Jingyu Zhang [1,2], Rui Sun [1,2,3,*], Zhiqiang Xiao [1,2], Liang Zhao [1,2] and Donghui Xie [1,2]

[1] State Key Laboratory of Remote Sensing Science, Faculty of Geographical Science, Beijing Normal University, Beijing 100875, China; 201931051036@mail.bnu.edu.cn (J.Z.); zhqxiao@bnu.edu.cn (Z.X.); 202031051039@mail.bnu.edu.cn (L.Z.); xiedonghui@bnu.edu.cn (D.X.)
[2] Beijing Engineering Research Center for Global Land Remote Sensing Products, Faculty of Geographical Science, Beijing Normal University, Beijing 100875, China
[3] Faculty of Arts and Sciences, Beijing Normal University, Zhuhai 519087, China
* Correspondence: sunrui@bnu.edu.cn

Abstract: The leaf area index (LAI) is a crucial variable in climate, ecological, and land surface modeling. However, the estimation of the LAI from coarse-resolution remote sensing data can be affected by the spatial scaling bias, which arises from the nonlinearity of retrieval models and the heterogeneity of the land surface. This study provides an algorithm named Arithmetic Mean and Geometric Mean (AM–GM) to correct the spatial scaling bias. It is established based on negative logarithmic functions and avoids second-order stationarity. In this algorithm, relationships are derived between the scaling bias of LAI and the arithmetic and geometric means of directional gap probability for two commonly used remote sensing models, the Beer–Lambert law and a semi-empirical transfer function, respectively. According to the AM–GM algorithm, the expression representing the model nonlinearity is derived and utilized for the analysis of LAI scaling bias. Furthermore, the AM–GM algorithm is simplified by a linear relationship, which is constructed between two quantities related to the directional gap probability between two specific resolutions. Two scenes simulated by the LargE-Scale remote sensing data and image Simulation framework (LESS) model and three sites are used to evaluate the proposed algorithm and analyze the scaling bias of LAI. The validation results show that the AM–GM algorithm provides accurate correction of LAI scaling bias. The analyses based on the AM–GM algorithm demonstrate that the scaling bias of LAI increases with the increase in the LAI value, with stronger surface heterogeneity and coarser spatial resolution. The validation results of the simplified AM–GM algorithm demonstrate that at the Sud-Ouest site, the absolute value of the bias for the estimated LAI decreases from 0.10, 0.22, 0.29, and 0.31 to 0.04, 0.01, 0.04, and 0.05 at 200 m, 500 m, 1000 m, and 1500 m resolutions, respectively. In conclusion, the proposed algorithm is effective in the analysis and correction of the scaling bias for coarse-resolution LAI.

Keywords: leaf area index (LAI); spatial scaling bias; coarse resolution; Arithmetic Mean and Geometric Mean (AM–GM); Taylor series expansion method (TSEM)

Citation: Zhang, J.; Sun, R.; Xiao, Z.; Zhao, L.; Xie, D. AM–GM Algorithm for Evaluating, Analyzing, and Correcting the Spatial Scaling Bias of the Leaf Area Index. *Remote Sens.* **2023**, *15*, 3068. https://doi.org/10.3390/rs15123068

Academic Editor: Lin Du

Received: 24 April 2023
Revised: 27 May 2023
Accepted: 8 June 2023
Published: 12 June 2023

1. Introduction

The leaf area index (LAI) is an essential variable in ecological, land surface, and climate modeling, as it explains the transfer of water, carbon, and energy between vegetation and the atmosphere [1,2]. The LAI is defined as one-half of the total green leaf area per unit of horizontal ground surface area [3]. In recent years, much research has applied coarse-resolution LAI (250 m–1000 m) to comprehend global vegetation change [4,5] and ecosystem productivity [6,7]. However, the accurate estimation of LAI at coarse resolution using remote sensing methods has been challenging due to the scaling effect [8].

The scaling effect is caused by model nonlinearity and surface heterogeneity. Most retrieval functions are nonlinear and built at a local scale (fine resolution) [9,10], which only interprets the surface heterogeneity at the corresponding scale [11,12]. When these

functions are applied to a coarse spatial resolution, the scaling effect causes spatial scaling bias of LAI estimation [13,14]. Yin et al. reported that the scaling bias in LAI inversion can reach up to 26% [15]. Hence, scaling bias is an important consideration for the LAI estimated from coarse-resolution remote sensing data, especially on a heterogeneous surface [16–18].

To deal with this task, previous studies have proposed several methods. On the one hand, statistical regression relationships have been developed to calculate the spatial scaling bias [19,20]. For example, Zhao and Fan established a statistical regression relationship between a spatial heterogeneity coefficient and the scaling bias of LAI. However, empirical methods require external factors that limit their applicability. On the other hand, a series of universal methods have been provided [8,21–26]. For instance, the computational geometry method (CGM) sets the upper and lower envelopes of the retrieval model to achieve accurate parameter estimation at coarse resolutions [21]. The advantage of this method is that it is not affected by the continuity of the remote sensing model and does not require high-resolution remote sensing data. However, the true distribution of parameters is not considered. Chen et al. addressed the limitations of the CGM algorithm by introducing variable weights instead of fixed weights [26]. Nevertheless, the inherent flaw of the CGM method—its inability to express the scaling bias using a formula—has yet to be resolved. Similarly, machine learning models estimated parameters at coarse resolution based on the relationships built at a fine resolution, and the accuracy of the inversion parameter was controlled by the reference parameters at a coarse resolution [27]. Such methods are not suitable for analyzing scaling bias because a relevant formula cannot be established. The Taylor series expansion method (TSEM) is another universal method in which each term has a physical meaning [22]. This method is helpful for analyzing scaling bias. However, the arithmetic mean of the input variable for the LAI retrieval models is used to derive the second derivative term in the TSEM, which also ignores the true distribution of parameters [10,28]. This method also requires synchronous fine-resolution remote sensing data. Later, Garrigues et al. extended the TSEM algorithm to a multivariate transfer function but still left the problem unresolved [8]. Recently, several upscaling models are proposed based on fractal theory [23–25]. A number of studies have attempted to explain the fractal dimension [29], but no consensus has been reached. In summation, the TSEM algorithm is more suitable for analyzing and correcting the scaling bias, but the algorithm itself is limited by second-order stationarity and fine-resolution data.

TSEM is closely related to the model type [30]. In mathematics, scaling bias is referred to as negative Holder's defect. When the model form is a negative logarithmic function, Holder's defect can be accurately expressed by utilizing the arithmetic and geometric means of the input variables [31]. Hence, the negative logarithmic functions can be employed to develop a method for calculating and correcting the scaling bias. Two commonly used LAI inversion models with negative logarithmic form, the Beer–Lambert law [32] and a semi-empirical transfer function that establishes the relationship between the normalized difference vegetation index (NDVI) to LAI [33], are employed in this research. Notably, the equation for NDVI related to reflectance is nonlinear, leading to the scaling bias of NDVI on heterogeneous surfaces [8,34]. This bias not only affects the scaling bias calculation but also hinders the analysis of the scaling bias and the comprehensive understanding of the scaling effect.

In this study, an Arithmetic Mean and Geometric Mean (AM–GM) algorithm is proposed to deeply analyze and correct the LAI scaling bias. The algorithm aims to solve the inherent flaws of the TSEM. The practicality of this algorithm is enhanced by establishing a linear relationship between two specific resolutions, eliminating the need for fine-resolution remote sensing data.

2. Materials

In this study, data are obtained from both simulated scenes and in situ sites to validate the algorithm and analyze the scaling bias of LAI. The LargE-Scale remote sensing data and image Simulation framework (LESS) model were employed to simulate heterogeneous

3D scenes [35]. The in situ data were downloaded from the VAlidation of Land European Remote-sensing Instruments (VALERI) project (http://w3.avignon.inra.fr/valeri/, accessed on 15 March 2023). Two simulated scenes and three in situ sites are used to analyze and validate the proposed algorithm, and the land cover type includes cropland and forest. Four additional cropland sites are selected to simplify the AM–GM algorithm. At simulated scenes, the data are simulated at 1 m and then aggregated to 5 m, 9 m, 15 m, and 45 m. At the VALERI sites, the data are obtained at 20 m spatial resolution and aggregated to 200 m, 500 m, 1000 m, 1500 m, and 3000 m.

2.1. Simulated Data

Two 3D forest scenes are constructed using the LESS model in this paper, as shown in Figure 1. Both scenes have an area of 45 m × 45 m. The first scene consists of 581 trees. These trees are derived from 42 single-tree models, simulated by 6 different canopy shapes and 7 levels of leaf area index. Each tree's position is determined based on field measurements. The LAI of the whole scene is 2.67. For more detailed information on the scene construction, please refer to Scene S4, which was constructed by Xu et al. [36]. Additionally, a virtual forest scene with stronger surface heterogeneity is constructed from the same single-tree models and different numbers of trees. The LAI of this virtual scene is 2.14. The spectral information of leaves and soil has been measured on the ground by Xu et al. [36]. The data simulations are performed with an observation zenith angle of 0°. Detailed parameter settings can be found in Table 1.

Table 1. Parameter settings of the LESS model.

Sensor	**Parameter Value**	**Optical Database**	**Parameter Value**
Type	Orthographic	Larch Branch	Ground Measurements
Width (pixels)	45	Brown Loam	Ground Measurements
Height (pixels)	45	Larch Leaf	Ground Measurements
Samples (/pixel)	64	**Terrain**	**Parameter Value**
Spectral Bands	482:60, 561.5:57, 654.5:37, 865:28	Type	Plane
Image Format	Spectrum	XSize (m)	45
NoData Value	−1	YSize (m)	45
Width Extent (m)	45	BRDF Type	Lambertian
Height Extent (m)	45	Optical Property	Brown Loam
Four Components Product	Tick		
Observation	**Parameter Value**	**Objects**	**Parameter Value**
View Zenith (°)	0	Single-Tree Models of Larch	Constructed by Xu et al. [36]
View Azimuth (°)	180		
Sensor Height (m)	30		
Illumination and Atmosphere	**Parameter Value**	**Advanced**	**Parameter Value**
Sun Zenith (°)	30	Minimum Iterations	5
Sun Azimuth (°)	90	Number of Cores	20
Sky-Type	SKY_TO_TOTAL		
Sky-Percentage	0, 0		

Over the simulated scenes, the directional gap probabilities are calculated from four component products, which are simulated using the LESS model:

$$p(\theta) = p_{is} + p_{ss} \quad (1)$$

where p_{is} and p_{ss} represent the proportions of illuminated soil and shaded soil within each pixel, respectively. At a spatial resolution of 1 m, the directional gap probabilities are simulated. The results are then aggregated to coarser spatial resolutions of 5 m, 9 m, 15 m, and 45 m.

Figure 1. Standard false-color images of two forest scenes simulated using the LESS model: (**a**) Genhe scene; (**b**) virtual scene.

2.2. Site Data

Seven VALERI sites are used and the data of these sites are downloaded from the VALERI website (Figure 2). To validate the algorithm and analyze the scaling bias, three sites are used. In particular, the vineyard dominates the Plan-de-Dieu site; Quercus ilex dominates the Puéchabon site; and the Sud-Ouest site includes nine crops, including corn, soya, sunflower, harvest wheat, etc. To simplify the AM–GM algorithm, four additional cropland sites covered by a variety of crops are chosen, including Les Alpilles, Barrax, Demmin, and Haouz. Table 2 provides detailed information about these sites, including land cover, image acquisition time, site size, and location.

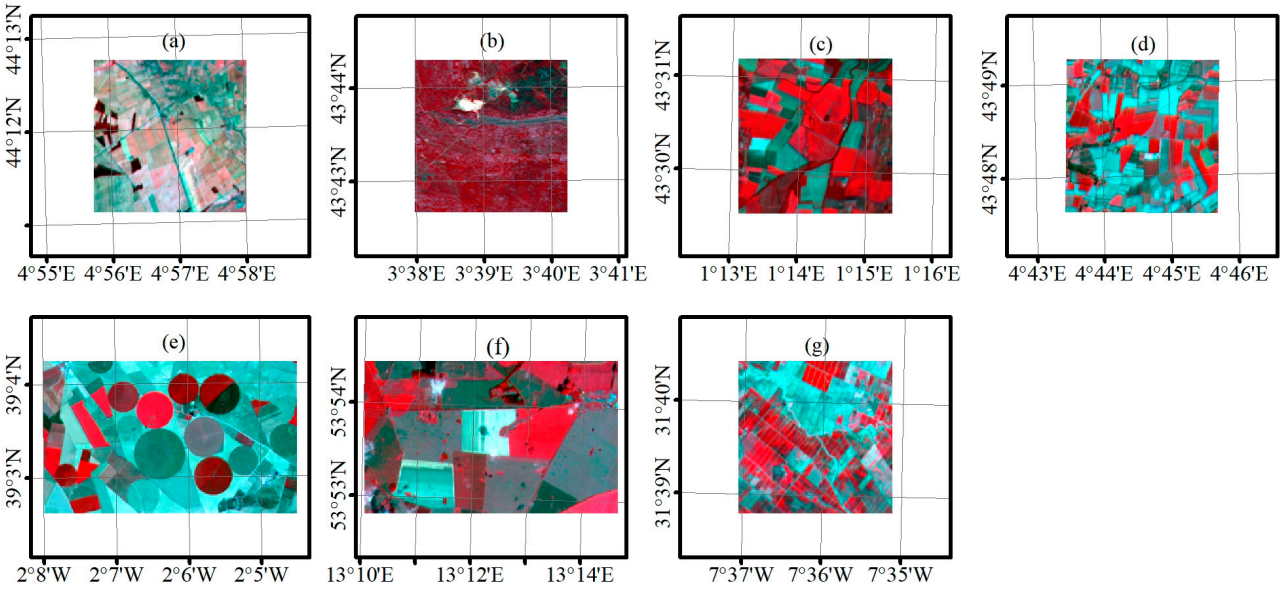

Figure 2. Standard false-color images of the VALERI sites: (**a**) Plan-de-Dieu; (**b**) Puéchabon; (**c**) Sud-Ouest; (**d**) Les Alpilles; (**e**) Barrax; (**f**) Demmin; (**g**) Haouz.

Table 2. Detailed information of the VALERI sites.

Site Name	Land Cover	Day of Year	Image Year	Spatial Resolution	Site Size	Location
Plan-de-Dieu	Crops	181	2004	20 m	3 km × 3 km	44°11′N, 4°56′E
Puéchabon	Mediterranean Forests	163	2001	20 m	3 km × 3 km	43°43′N, 3°38′E
Sud-Ouest	Nine Crops	201	2002	20 m	3 km × 3 km	43°30′N, 1°14′E
Les Alpilles	Crops	204	2002	20 m	3 km × 3 km	43°48′N, 4°42′W
Barrax	Crops	195	2003	20 m	5 km × 3 km	39°40′N, 2°60′W
Demmin	Crops	164	2004	20 m	5 km × 3 km	53°53′N, 13°12′E
Haouz	Crops	73	2003	20 m	3 km × 3 km	31°39′N, 7°36′W

Near-infrared (ρ_{NIR}) and red (ρ_R) reflectances are obtained from SPOT images, which have a spatial resolution of 20 m. These data are aggregated to coarser resolutions (200 m, 500 m, 1000 m, 1500 m, and 3000 m), then NDVI and directional gap probability are computed at those spatial resolutions. The in situ LAI data are also downloaded to build the retrieval model at 20 m spatial resolution.

3. Methods

In this study, a novel algorithm called AM–GM is proposed to more accurately evaluate, analyze, and correct the scaling bias of LAI. This algorithm utilizes the advantage of negative logarithmic functions to avoid the second-order stationarity hypothesis, and this algorithm considers the scaling bias of NDVI. Moreover, the practicality of this algorithm is improved by eliminating the requirement for fine-resolution remote sensing data. In particular, the relationship between the LAI scaling bias and the arithmetic and geometric means of directional gap probability is investigated based on negative logarithmic functions. This relationship is exploited to derive the LAI scaling bias. In addition, the AM–GM algorithm uses Taylor's theorem [22,31] to indirectly calculate the accurate values of the second derivative term, obtaining conditions for in-depth analysis of the model nonlinearity. Lastly, statistical relationships are established between two quantities related to directional gap probability between two specific scales for cropland. The flowchart depicting this process is shown in Figure 3.

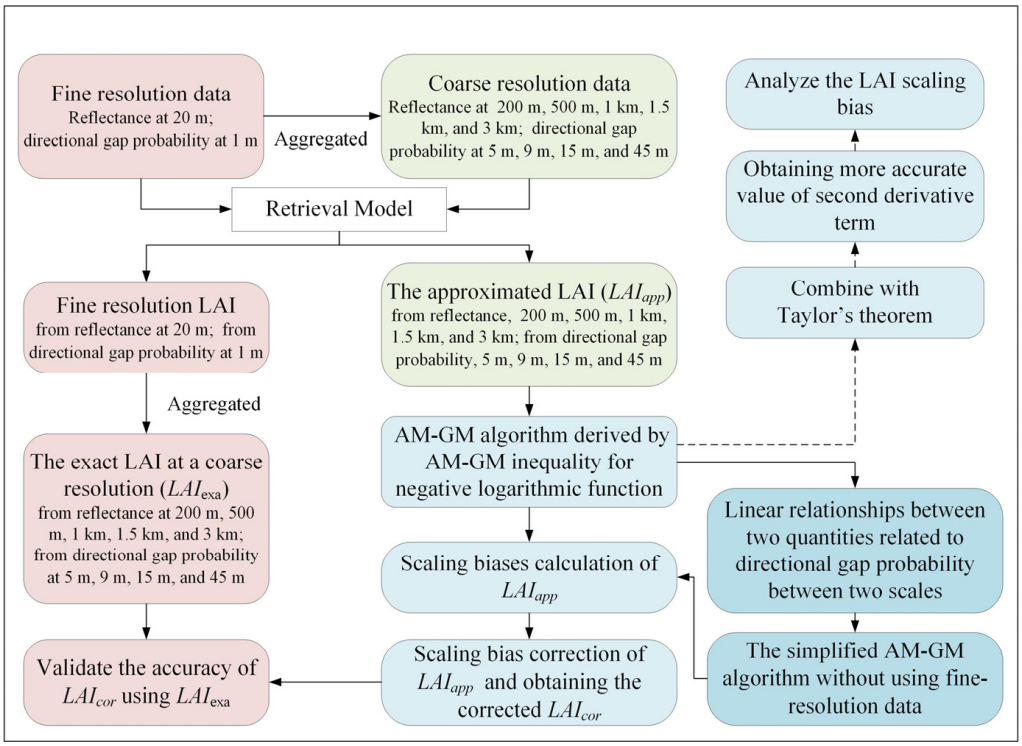

Figure 3. The flowchart for calculating, analyzing, and correcting the scaling bias of LAI using the AM–GM algorithm.

3.1. Mathematical Theory of the AM–GM Algorithm

3.1.1. Holder's Defect and AM–GM Inequality

In the field of mathematics, suppose that $X = \{x_1, x_2, \ldots, x_N\}$ is a random variable and model f is twice continuously differentiable. The value estimated by the expected value of X based on the function f is denoted by $f(E(X))$, and the expected value of the function is denoted by $E(f(X))$. Holder's defect (Δ) is used to express the discrepancy between the two terms [31]:

$$\Delta = E(f(X)) - f(E(X)) = \frac{1}{2}\mu Var(X) \tag{2}$$

where $Var(X)$ is the variance of X, and there exists a real value μ for the above formula. When f is a negative logarithmic function, the AM–GM inequality associated with random variable X can be given an explicit formula following Holder's defect [31].

$$\begin{aligned} -\ln(\tfrac{x_A}{x_G}) &= -\ln(x_A) - (-\ln(x_G)) = -\ln\left(\tfrac{1}{N}\sum_{k=1}^{N} x_k\right) - \left(-\ln\left(\sqrt[N]{\prod_{k=1}^{N} x_k}\right)\right) \\ &= -\ln\left(\tfrac{1}{N}\sum_{k=1}^{N} x_k\right) - \tfrac{1}{N}\sum_{k=1}^{N}(-\ln(x_k)) = f(E(X)) - E(f(X)) = -\Delta \end{aligned} \tag{3}$$

where x_A is the arithmetic mean of X; x_G is the geometric mean of X; $x_k \in X$; N is a natural number; k is equal to 1 to N. Accordingly, Holder's defect can be expressed by the AM–GM inequality, as follows:

$$\Delta = \ln\left(\frac{x_A}{x_G}\right) \tag{4}$$

3.1.2. Calculation of LAI Scaling Bias

The LAI retrieval model f is constructed at fine spatial resolution. Applying f to fine-resolution data, then aggregating the resulting data to coarse resolution, yields the exact LAI (LAI_{exa}). The LAI_{exa} is the reference LAI at coarse resolution because leaf area follows the law of conservation of matter [10]. The approximate LAI (LAI_{app}) is obtained by applying model f to coarse-resolution data, which are aggregated from fine-resolution data. The difference between LAI_{app} and LAI_{exa} is the spatial scaling bias [23], as shown in Figure 4.

In the field of remote sensing, according to Equations (2) and (4), the real scaling bias of the inverted parameter can be expressed as follows:

$$bias_{Real} = LAI_{app} - LAI_{exa} = f(E(X)) - E(f(X)) = -\Delta = -\ln\left(\frac{x_A}{x_G}\right) \tag{5}$$

Next, two LAI retrieval models with negative logarithmic form are used to derive the scaling bias of LAI.

The Beer–Lambert law is a negative logarithmic function [37,38]:

$$LAI = -\frac{\cos\theta}{\Omega G(\theta)}\ln(p(\theta)) \tag{6}$$

where $G(\theta)$ represents the leaf projection coefficient on a plane perpendicular to the observation direction θ. θ is set to 30 degrees in Table 1. Assuming that foliage angles are distributed spherically, $G(\theta)$ is set to 0.5 [39]. Ω is the foliage clumping index, which is set as a constant according to the vegetation type [40,41]. Here, fine-resolution directional gap probability $p(\theta)$ is measured based on geometric features, and there is no scaling effect [42]. According to Equations (5) and (6), the scaling bias of LAI is:

$$bias_{AM-GM} = -\frac{\cos\theta}{\Omega G(\theta)}\ln\left(\frac{A[p(\theta)]}{G[p(\theta)]}\right) \tag{7}$$

where $G[p(\theta)]$ and $A[p(\theta)]$ are the geometric and arithmetic means of fine resolution $p(\theta)$ within a coarse-resolution pixel, respectively.

The NDVI-LAI semi-empirical transfer function also has a negative logarithmic form [43],

$$LAI = -\frac{1}{K_{LAI}}\ln\left(\frac{NDVI - NDVI_{\max}}{NDVI_{\min} - NDVI_{\max}}\right) \tag{8}$$

where $NDVI_{\max}$ is the asymptotic value of NDVI, which is obtained when LAI is greater than 8; $NDVI_{\min}$ is the NDVI value for bare soil; K_{LAI} represents the extinction coefficient, which relates to vegetation spatial structure and vegetation canopy structure [33,44]. Here, the directional gap probability is obtained using Equation (9) [41]:

$$p(\rho_{NIR}, \rho_R) = \frac{\frac{\rho_{NIR} - \rho_R}{\rho_{NIR} + \rho_R} - NDVI_{\max}}{NDVI_{\min} - NDVI_{\max}} \tag{9}$$

where ρ_{NIR} and ρ_R represent near-infrared and red reflectances, respectively. To avoid introducing the scaling bias of NDVI into the directional gap probability calculation at coarse resolution, we use the aggregated reflectance rather than the aggregated NDVI. According to Equations (5) and (8), the scaling bias of LAI is:

$$bias_{\rho\_AM-GM} = -\frac{1}{K_{LAI}} \ln\left(\frac{p(A[\rho_{NIR}], A[\rho_R])}{G[p(\rho_{NIR}, \rho_R)]}\right) \tag{10}$$

where $G[p(\rho_{NIR}, \rho_R)]$ is the geometric mean of fine resolution $p(\rho_{NIR}, \rho_R)$ within a coarse-resolution pixel, and $p(A[\rho_{NIR}], A[\rho_R])$ is the directional gap probability at coarse resolution estimated based on the arithmetic mean of the fine-resolution reflectance.

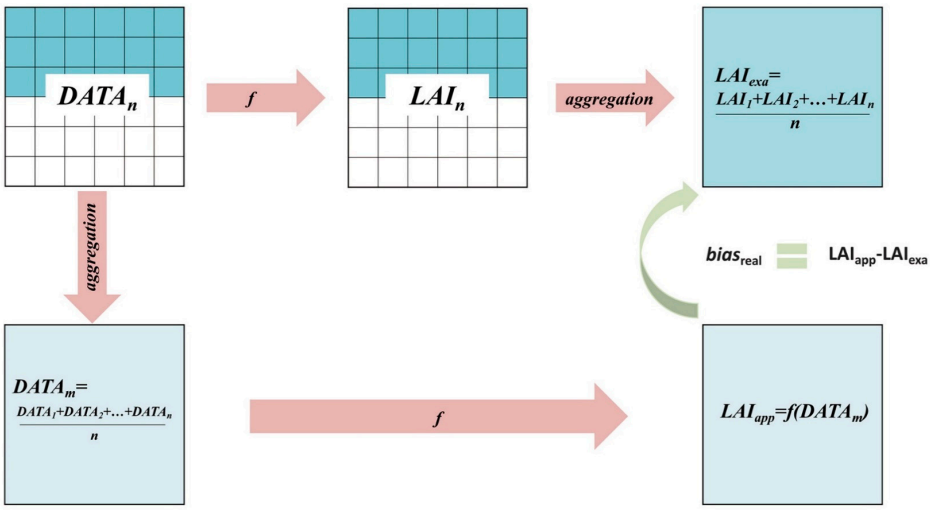

Figure 4. Schematic diagram of the scaling bias of LAI at coarse resolution in quantitative remote sensing. The LAI retrieval model f is built at fine resolution. $DATA_n$ represents the fine-resolution remote sensing data, and their corresponding LAI values at fine resolution (LAI_n) are retrieved using f. LAI_{exa} represents the exact LAI at coarse resolution; this is acquired by averaging LAI_n. $DATA_m$ represents the coarse-resolution remote sensing data, which is obtained by averaging $DATA_n$. LAI_{app} represents the approximate LAI at coarse resolution, which is obtained by applying model f to data $DATA_m$. $bias_{real}$ represents the LAI scaling bias of a coarse resolution pixel, indicated by the difference between LAI_{app} and LAI_{exa}.

3.2. Calculate Factor μ

The second derivative term μ absorbs the impact of all higher-order moments associated with X in Equation (2). $p(\theta)$ is measured according to the canopy geometry [45], the value at coarse resolution is equal to the arithmetic mean of fine-resolution directional gap probability $p(\theta)$. The value of μ can be derived directly from Equation (2). It can also be obtained using the second derivative. Therefore, the μ value based on Equation (6) is shown as follows:

$$\mu_{AM-GM} = -\frac{2bias_{AM-GM}}{Var(X)} = \frac{1}{\frac{\Omega G(\theta)}{\cos\theta} \times {c_k}^2} \tag{11}$$

where c_k is related to $p(\theta)$.

When the directional gap probability calculation involves a nonlinear model, such as Equation (8), the value of $p(A[\rho_{NIR}], A[\rho_R])$ is not equal to the value of $A[p(\rho_{NIR}, \rho_R)]$ (the arithmetic mean of fine-resolution $p(\rho_{NIR}, \rho_R)$). The first-order derivative term cannot be eliminated. Thus, Equation (2) is modified as follows:

$$\Delta = \frac{1}{2}\mu_{\rho\_AM-GM}Var(X) + f'\left(x^M\right)\sum_{k=1}^{N}\frac{\left(x_k - x^M\right)}{N} \tag{12}$$

where x_k is the kth value of $p(\rho_{NIR}, \rho_R)$ within a coarse-resolution pixel; x^M represents the directional gap probability at coarse resolution, i.e., $p(A[\rho_{NIR}], A[\rho_R])$; μ_{ρ_AM-GM} is the second derivative term and $Var(X)$ is the mean square error. According to Equations (10) and (12), the value of μ based on Equation (8) can be expressed as follows:

$$\mu_{\rho\_AM-GM} = -\frac{2\left(bias_{\rho\_AM-GM} + f'\left(x^M\right)\frac{\sum_{K=1}^{N}\left(x_k - x^M\right)}{N}\right)}{Var(X)} = \frac{1}{k_{LAI} \times {c_k}^2} \tag{13}$$

where c_k is related to $p(\rho_{NIR}, \rho_R)$.

3.3. Simplify the AM–GM Algorithm

The application of the AM–GM algorithm is limited by its use of fine-resolution remote sensing data. In this section, this algorithm was simplified. According to Equation (A4) in Appendix A and Equation (10), the following formula can be derived:

$$bias_{\rho\_AM-GM} = LAI_{app} \times \left(1 - \frac{\ln\left(G[p(\rho_{NIR}, \rho_R)]\right)}{\ln\left(p(A[\rho_{NIR}], A[\rho_R])\right)}\right) \tag{14}$$

where $\ln\left(p(A[\rho_{NIR}], A[\rho_R])\right)$ represents the logarithm of the directional gap probabilities at coarse resolution and $\ln\left(G[p(\rho_{NIR}, \rho_R)]\right)$ represents the logarithm of the geometric mean of fine resolution $p(\rho_{NIR}, \rho_R)$ within a coarse-resolution pixel.

A linear relationship between $\ln\left(p(A[\rho_{NIR}], A[\rho_R])\right)$ and $\ln\left(G[p(\rho_{NIR}, \rho_R)]\right)$ was found between two specific resolutions; the relationship will be described in further detail in the Results section. Equation (14) can be simplified according to the linear relationship, as follows:

$$bias_{\rho\_AM-GM} = LAI_{app} \times \left(\frac{b}{\ln\left(p(A[\rho_{NIR}], A[\rho_R])\right)} - a\right) \tag{15}$$

where parameters a and b are constants between two specific resolutions. According to Equation (15), the scaling bias of LAI can be calculated based on the coarse resolution data.

4. Results

4.1. Validation Results of the AM–GM Algorithm

Firstly, this study validates the correction effectiveness of the AM–GM algorithm when the Beer–Lambert law is the LAI retrieval model. The computation of LAI scaling bias based on the Beer–Lambert law is derived in Equation (7). Figure 5 and Table 3 show the magnitude of the scaling bias before and after correction. Before the correction, the retrieval LAI_{app} at coarse resolution exhibits significant negative scaling biases (bias = −0.67 and bias = −0.62). After correction, the bias and RMSE values between LAI_{cor} and LAI_{exa} are both reduced to almost 0. Furthermore, the spatial distribution of the corrected values LAI_{cor} coincides with LAI_{exa}. These results indicate that the AM–GM algorithm is effective when the Beer–Lambert law is the retrieval model.

We also assess the correction effectiveness when the NDVI-LAI semi-empirical transfer function is the LAI retrieval model. The equation for the calculation of LAI scaling

bias is shown in Equation (10). Figure 6 and Table 3 show that the scaling biases are small at the Plan-de-Dieu site, with RMSE = 0.05 and bias = −0.03; moderate at the Puéchabon site, with RMSE= 0.19 and bias = −0.14; and high at the Sud-Ouest site, with RMSE = 0.25 and bias = −0.22. After correction, the values of RMSE and bias between LAI_{cor} and LAI_{exa} are also deduced to almost 0, and all spots are clustered on the 1:1 line. Meanwhile, the spatial distributions of LAI_{cor} coincide with LAI_{exa}. These results indicate that the AM–GM algorithm is effective when the NDVI-LAI semi-empirical transfer function is the retrieval model.

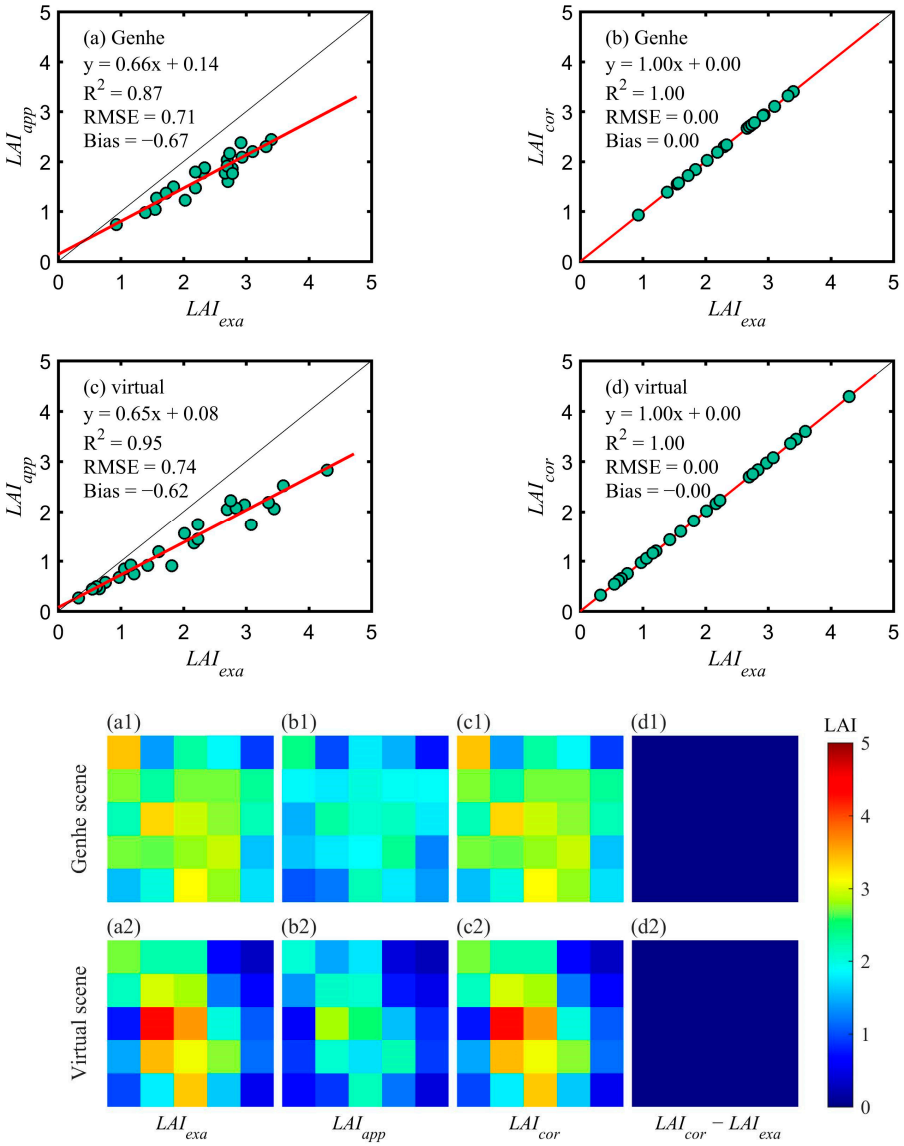

Figure 5. Numerical and spatial correction effectiveness of the AM–GM algorithm over two simulated scenes. The exact LAI (LAI_{exa}, m^2/m^2) at 9 m spatial resolution is obtained from directional gap probability at 1 m spatial resolution and then aggregated to 9 m spatial resolution; the approximated LAI at 9 m spatial resolution (LAI_{app}, m^2/m^2) is evaluated from the aggregated directional gap probability at 9 m spatial resolution. The corrected LAI_{app} (LAI_{cor}, m^2/m^2) are achieved using the AM–GM algorithm at 9 m spatial resolution. The errors between LAI_{app} and LAI_{exa} over (**a**) the Genhe scene and (**c**) the virtual scene; the errors between LAI_{cor} and LAI_{exa} over (**b**) the Genhe scene and (**d**) the virtual scene. (**a1**–**d1**) spatial distributions of LAI_{exa}, LAI_{app}, LAI_{cor}, and the difference between LAI_{exa} and LAI_{cor} over the Genhe scene; (**a2**–**d2**) spatial distributions of LAI_{exa}, LAI_{app}, LAI_{cor}, and the difference between LAI_{exa} and LAI_{cor} over the virtual scene.

Table 3. LAI scaling bias before and after correction at 500 m spatial resolution.

Site Name	Before Correction		After Correction	
	RMSE	Bias	RMSE	Bias
Genhe	0.71	−0.67	0.00	0.00
Virtual	0.74	−0.62	0.00	0.00
Plan-de-Dieu	0.05	−0.03	0.00	0.00
Puéchabon	0.19	−0.14	0.00	0.00
Sud-Ouest	0.25	−0.22	0.00	0.00

4.2. Analysis of LAI Scaling Bias

Two figures are used to analyze the LAI scaling bias based on three aspects: spatial resolution, model nonlinearity, and surface heterogeneity. In Figure 7, we calculate the average of LAI scaling bias for each scene and site using the AM–GM algorithm at multiple scales. In Figure 8, the values of μ and $Var(X)$ are calculated for each coarse pixel based on Equations (11) and (13).

- Spatial resolution.

When the spatial resolution for LAI estimation becomes coarser, the scaling bias of LAI increases. The scaling bias of LAI between two close resolutions may also be large. In Figure 7, as the spatial resolution moves from 1 to 45, the value of LAI scaling bias decreases and the LAI scaling bias increases. For the Beer–Lambert law, the scaling bias of LAI_{app} at 5 m spatial resolution relative to LAI_{exa} estimated at 1 m spatial resolution is large, as shown in Figure 7a.

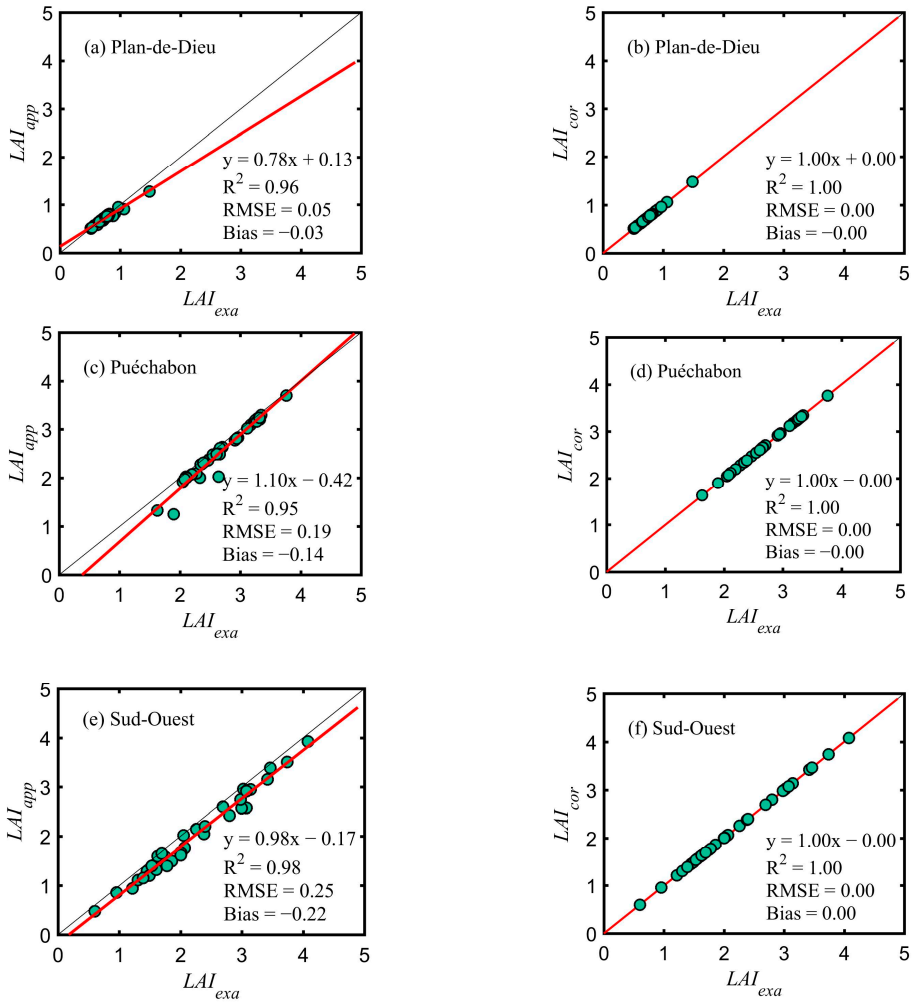

Figure 6. *Cont.*

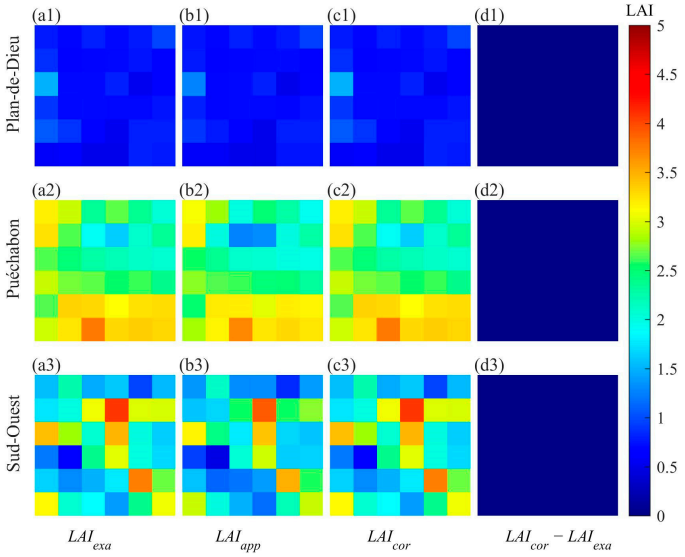

Figure 6. Numerical and spatial correction effectiveness of the AM–GM algorithm over three VALERI sites. The exact LAI (LAI_{exa}, m^2/m^2) at 500 m spatial resolution is obtained from reflectance at 20 m spatial resolution and then aggregated to 500 m spatial resolution. The approximate LAI (LAI_{app}, m^2/m^2) at 500 m spatial resolution is estimated from the aggregated reflectance at 500 m spatial resolution. The corrected LAI_{app} (LAI_{cor}, m^2/m^2) is achieved using the AM–GM algorithm at 500 m spatial resolution. The errors between LAI_{app} and LAI_{exa} over (**a**) the Plan-de-Dieu site, (**c**) the Puéchabon site, and (**e**) the Sud-Ouest site; the errors between LAI_{cor} and LAI_{exa} over (**b**) the Plan-de-Dieu site, (**d**) the Puéchabon site, and (**f**) the Sud-Ouest site. (**a1**–**d1**) spatial distributions of LAI_{exa}, LAI_{app}, LAI_{cor}, and the difference between LAI_{exa} and LAI_{cor} over the Plan-de-Dieu site; (**a2**–**d2**) spatial distributions of LAI_{exa}, LAI_{app}, LAI_{cor}, and the difference between LAI_{exa} and LAI_{cor} over the Puéchabon site; (**a3**–**d3**) spatial distributions of LAI_{exa}, LAI_{app}, LAI_{cor}, and the difference between LAI_{exa} and LAI_{cor} over the Sud-Ouest site.

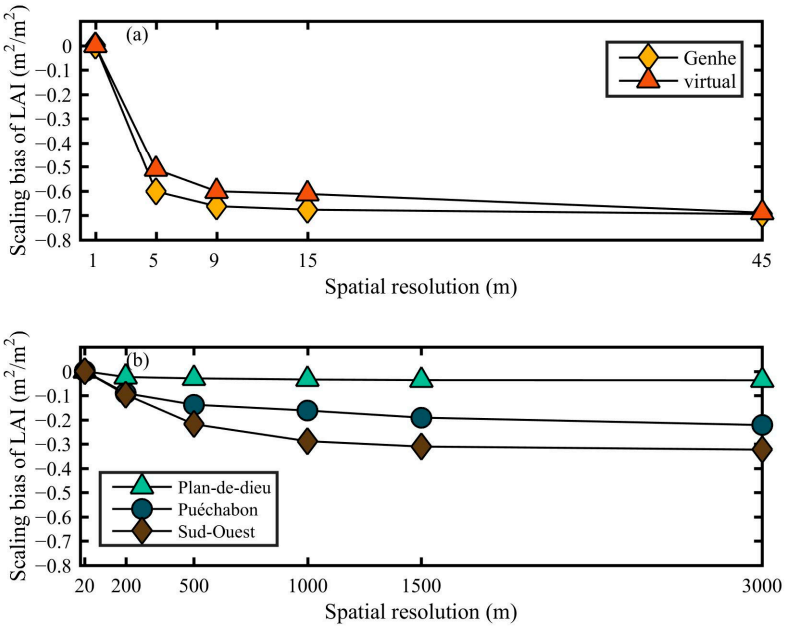

Figure 7. Average of LAI scaling bias calculated using the AM–GM algorithm at multiple scales for each scene and site: (**a**) based on the Beer–Lambert Law at two LESS simulated scenes, and (**b**) based on the NDVI-LAI semi-empirical transfer function at three VALERI sites.

- Model nonlinearity.

When the LAI value increases, the degree of model nonlinearity also rises. This is because the model nonlinearity is related to $1/{c_k}^2$ in Equations (11) and (13), and the value of c_k is related to directional gap probability. When the value of c_k for a coarse pixel is small, the directional gap probability of this pixel is also small, and the LAI value is large [46]. For example, in Figure 6, the exact LAI values for row 2 to 4 in the fourth column of the Sud-Ouest site are relatively large. Correspondingly, in Figure 8, the values of μ_{ρ_AM-GM} calculated by the AM–GM algorithm for these pixels are also relatively high.

- Surface heterogeneity.

When vegetation in a coarse pixel has different growing seasons, the degree of surface heterogeneity is high. The Sud-Ouest site includes nine crops with various growing seasons, while both the Plan-de-Dieu and Puéchabon sites have a relatively singular growing season. Therefore, Figure 8 shows that the $Var(X)$ values of the Sud-Ouest site are larger than those of the other two sites.

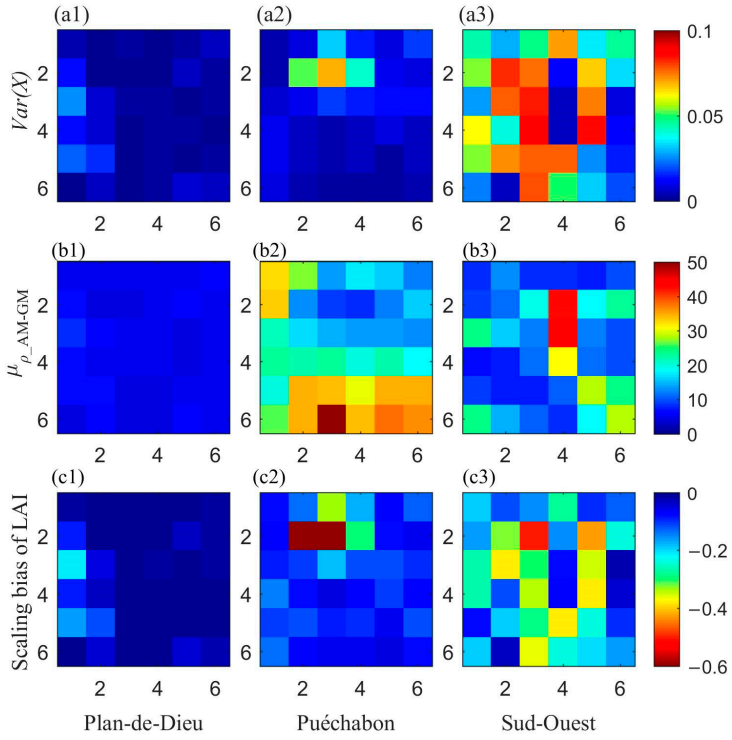

Figure 8. Spatial distribution maps of the LAI scaling bias and two factors ($Var(X)$ and μ_{ρ_AM-GM}) computed by the AM–GM algorithm based on the NDVI-LAI semi-empirical transfer function at 500 m resolution over three VALERI sites. (**a1**–**a3**) the local variance of directional gap probability at the Plan-de-Dieu site, the Puéchabon site, and the Sud-Ouest site, respectively. (**b1**–**b3**) the second derivative μ_{ρ_AM-GM} absorbs the impact of all higher-order moments at the Plan-de-Dieu site, the Puéchabon site, and the Sud-Ouest site, respectively. (**c1**–**c3**) the scaling bias of LAI at the Plan-de-Dieu site, the Puéchabon site, and the Sud-Ouest site, respectively.

4.3. Scaling Bias Calculated by the Simplified Algorithm

Although the AM–GM algorithm can correct the LAI scaling bias more accurately, it requires fine-resolution remote sensing data, which limits the applicability of this algorithm. The simplified AM–GM algorithm does not use fine-resolution data.

Figure 9 shows that linear relationships between the two quantities $\ln\left(p\left(A\left[\rho_{NIR}\right], A\left[\rho_R\right]\right)\right)$ and $\ln\left(G\left[p\left(\rho_{NIR}, \rho_R\right)\right]\right)$ are observed at four croplands between the fine and multiple resolutions (200 m, 500 m, 1000 m, and 1500 m), respectively. Due to the limited sample size, this relationship is not built at the spatial resolution of 3 km. The parameters a and b for simplified AM–GM algorithm in Equation (15) are shown in Table 4.

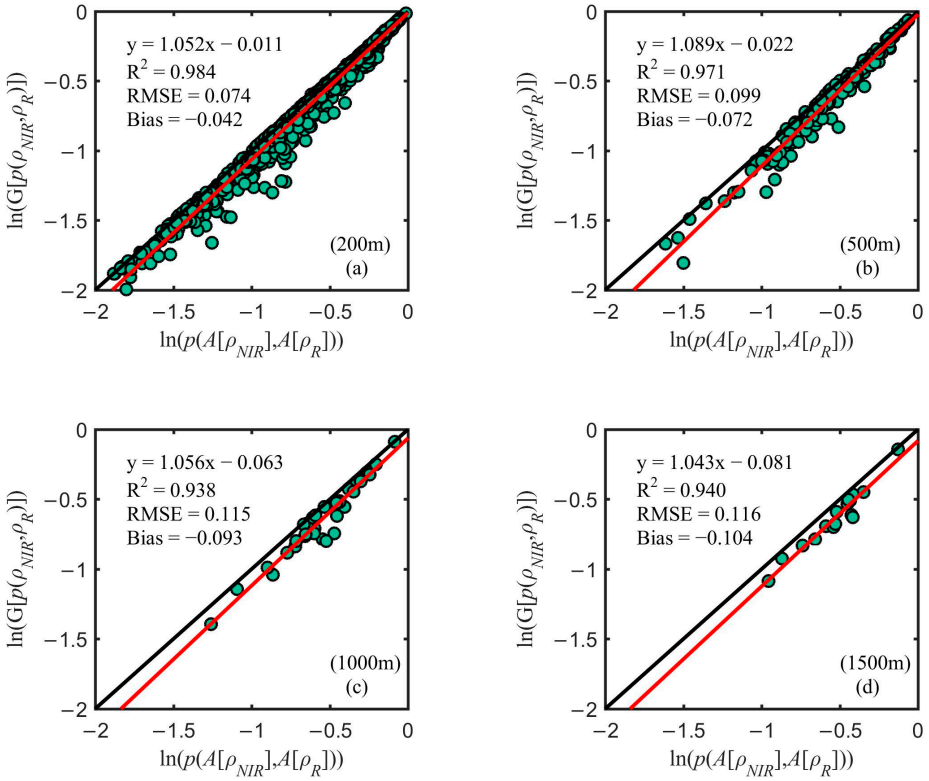

Figure 9. The statistical relationships between $\ln(G[p(\rho_{NIR},\rho_R)])$ and $\ln(p(A[\rho_{NIR}],A[\rho_R]))$ investigated at multiple resolutions, (**a**) 200 m, (**b**) 500 m, (**c**) 1000 m, and (**d**) 1500 m, over Les Alpilles, Barrax, Demmin, and Haouz cropland sites.

Table 4. The parameters *a* and *b* at multiple scales for the simplified AM–GM algorithm.

Parameters \ Spatial Resolution	200 m	500 m	1000 m	1500 m
a	0.052	0.089	0.056	0.043
b	0.011	0.022	0.063	0.081

The simplified AM–GM algorithm corrected the scaling bias of LAI at multiple scales over the Sud-Ouest site. Figure 10 shows that after correction, the values of LAI_{cor} are close to the values of LAI_{exa}. The absolute values of bias at the Sud-Ouest site decrease from 0.10, 0.22, 0.29, and 0.31 to 0.04, 0.01, 0.04, and 0.05 at 200 m, 500 m, 1000 m, and 1500 m, respectively. Moreover, Figure 11 shows that the spatial distributions of LAI_{cor} are well corrected, particularly at spatial resolutions of 1000 m and 1500 m. Therefore, the simplified AM–GM algorithm, which does not use fine-resolution images, is feasible.

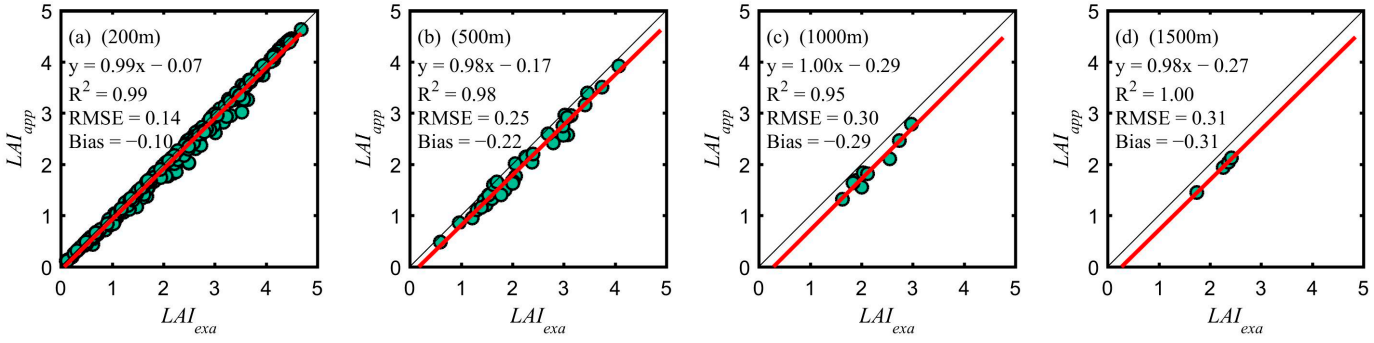

Figure 10. *Cont.*

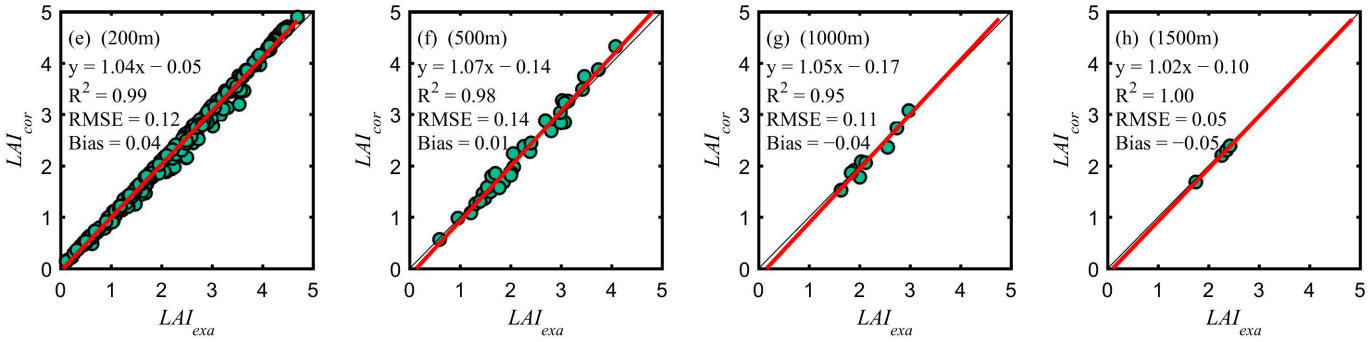

Figure 10. Correction of LAI scaling bias using the simplified AM–GM algorithm at multiple resolutions (200 m, 500 m, 1000 m, and 1500 m) over the Sud-Ouest site. Panels (**a**–**d**) show the errors between LAI_{app} and LAI_{exa} before correction, while panels (**e**–**h**) show the errors after correction.

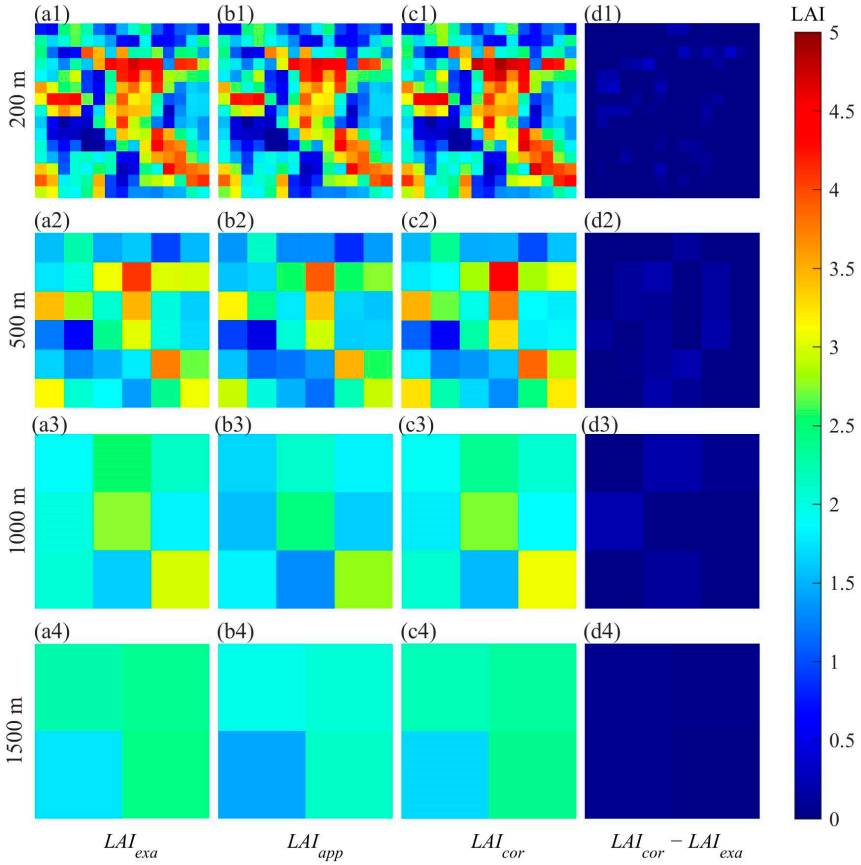

Figure 11. Spatial distributions of the exact LAI (LAI_{exa}), approximate LAI (LAI_{app}), corrected LAI (LAI_{cor}), and the differences between LAI_{cor} and LAI_{exa} at multiple resolutions (200 m, 500 m, 1000 m, and 1500 m) over the Sud-Ouest site. (**a1**–**d1**) represent LAI_{exa}, LAI_{app}, LAI_{cor}, and the difference between LAI_{cor} and LAI_{exa} at 200 m spatial resolution, respectively; (**a2**–**d2**) represent LAI_{exa}, LAI_{app}, LAI_{cor}, and the difference between LAI_{cor} and LAI_{exa} at 500 m spatial resolution, respectively; (**a3**–**d3**) represent LAI_{exa}, LAI_{app}, LAI_{cor}, and the difference between LAI_{cor} and LAI_{exa} at 1000 m spatial resolution, respectively; (**a4**–**d4**) represent LAI_{exa}, LAI_{app}, LAI_{cor}, and difference between LAI_{cor} and LAI_{exa} at 1500 m spatial resolution, respectively.

5. Discussion

5.1. Algorithm Comparison

Prior work has documented the flaws in the TSEM algorithm resulting from the second-order stationary hypothesis, which assumes that the mean of a random function

is a constant [30]. The AM–GM algorithm considered the higher-order moments, i.e., the skewness that measures the asymmetry, and the kurtosis that measures the heaviness of the tails of distribution without discarding [31]. We compared the values of μ calculated using the AM–GM and TSEM algorithms in Table 5. The results show bias in μ up to 7.16. However, the numerical discrepancies of the input variable used for μ calculation are less than 0.02. It is inferred that the μ value is sensitive to the input variable. On the heterogeneous surfaces, the skewness and kurtosis of the random variable may be large, and the AM–GM algorithm may exhibit a better performance for the computation of μ and LAI scaling bias.

Table 5. Model nonlinearity factor (μ) and input variable for the AM–GM and TSEM algorithms at 500 m resolution.

Site Name	μ		Input Variable	
	RMSE	Bias	RMSE	Bias
Plan-de-Dieu	5.56	−3.99	0.01	−0.00
Puéchabon	5.48	−4.58	0.02	−0.01
Sud-Ouest	13.43	7.16	0.02	0.01

In the improved CGM, the relative errors decreased from 3.35%, 11.01%, and 19.62% to an average of 0.28%, 1.48%, and 5.16%, respectively, at kilometer scales [26]. Jiang et al. indicated that the LAI scaling bias decreased to around 0.27 by the TSEM, Wavelet-Fractal (WF), and Fractal theory (TT) [30]. We determine that the AM–GM algorithm decreases the LAI scaling bias to almost zero. The simplified AM–GM algorithm decreases relative error from 16.07% to 4.3% at 1 km resolution. The LAI scaling bias decreases from 0.10, 0.22, 0.29, and 0.31 to 0.04, 0.01, 0.04, and 0.05 at 200 m, 500 m, 1000 m, and 1500 m resolutions, respectively. On the heterogeneous surfaces, the correction effect is comparable or even better. The simplified algorithm, TSEM, WF, or TT, does not perform well at homogeneous sites.

5.2. The Influence of NDVI Aggregation on the AM–GM Algorithm

To minimize errors of LAI estimation, care should be taken in relation to the scale issue of NDVI. In the past, studies usually used the vegetation index (VI) to calculate the scaling bias of LAI [30]. However, most of the equations for VIs are nonlinear, including the NDVI equation related to reflectance. The scaling bias of NDVI complicates the evaluation of the LAI scaling bias on the heterogeneous surface. Table 6 shows that the aggregated NDVI results in inaccurate estimates of LAI scaling bias based on the AM–GM algorithm. Additionally, the bias may be a positive or a negative value. In particular, several approaches have been provided to reconstruct time-series data for NDVI using both fine- and coarse-resolution NDVI data. The discussion in 5.2 may indicate that if the time-series data are used for LAI estimation, the scaling bias of NDVI should be considered during data reconstruction.

Table 6. Influence of NDVI aggregation on the AM–GM algorithm at 500 m resolution.

Site Name	Considering the Scaling Bias of NDVI		Ignoring the Scaling Bias of NDVI	
	RMSE	Bias	RMSE	Bias
Plan-de-Dieu	0.00	0.00	0.18	0.01
Puéchabon	0.00	0.00	0.49	0.04
Sud-Ouest	0.00	0.00	0.61	−0.08

5.3. Limitation of the AM–GM Algorithm

This algorithm is only suitable for negative logarithmic functions because Holder's defect provides an accurate expression of the AM–GM inequality for negative logarithmic functions [31]. This limitation restricts the application of the AM–GM algorithm. In

addition, this study corrected LAI scaling bias due to the spatial heterogeneity of vegetation growth but did not consider the model difference caused by vegetation types. In the future, we plan to further improve this algorithm for use with mixed land surfaces.

6. Conclusions

We found that scaling bias in remote sensing can be accurately expressed by the AM–GM inequality for negative logarithmic function. Based on this relationship, the AM–GM algorithm was proposed. This algorithm avoids the influence of the second-order stationary hypothesis. In addition, the aggregation of NDVI, which was ignored in previous research about scaling bias correction, is considered in the AM–GM algorithm. In this study, we validated the AM–GM algorithm at two simulated scenes and three sites, proving its effectiveness in the correction and analysis of the LAI scaling bias at coarse resolution.

In addition, upon analyzing the second derivative term, we identified a positive correlation between the LAI value and the degree of model nonlinearity. This means that as the LAI value increases, the nonlinearity in the model also increases. It was also observed that when the spatial resolution is coarse and the surface heterogeneity increases, there is a greater scaling bias in the LAI estimation. Adjusting for the LAI scaling bias was critical in the above three cases.

Furthermore, we identified a linear statistical relationship between two quantities related to directional gap probability between two specific scales. The AM–GM algorithm is simplified by the relationship. The results indicate that the simplified algorithm can practically correct the scaling bias without the requirement of fine-resolution remote sensing data. In conclusion, the correction effect of this algorithm is reliable. Future work includes the improvement of this algorithm on mixed land surfaces.

Author Contributions: Conceptualization, R.S.; Methodology, J.Z.; Validation, J.Z.; Formal analysis, J.Z.; Resources, D.X.; Writing—original draft, J.Z.; Writing—review & editing, R.S., Z.X. and L.Z.; Supervision, J.Z.; Funding acquisition, R.S. All authors have read and agreed to the published version of the manuscript.

Funding: This research was funded by the National Natural Science Foundation of China (42271330) and the National Key R&D Program of China (2021YFB3901201).

Data Availability Statement: The data presented in this study are available upon request from the corresponding author.

Acknowledgments: Thanks to Jialun Zhou (School of Electrical and Information Engineering, Zhengzhou university, China) for his contribution to the derivation of mathematical formulas.

Conflicts of Interest: The authors declare no conflict of interest.

Appendix A

Based on the Beer–Lambert law, the LAI_{exa} is estimated as follows:

$$LAI_{exa} = \frac{\sum_{k=1}^{N} -\frac{\cos\theta}{\Omega G(\theta)} \ln(p_k(\theta))}{N} = -\frac{\cos\theta}{\Omega G(\theta)} \ln(G[p_k(\theta)]) \quad \text{(A1)}$$

where N is the quantity of subpixels within a coarse resolution pixel; k is equal to 1 to N; foliage projection function $G(\theta)$ is set to 0.5; and $\cos\theta$ is set to 1. $G\left[p_k(\theta)\right]$ is the geometric mean of fine spatial resolution $p_k(\theta)$ within a coarse resolution pixel. LAI_{app} is:

$$LAI_{app} = -\frac{\cos\theta}{\Omega G(\theta)} \ln\left(\frac{\sum_{k=1}^{N} p_k(\theta)}{N}\right) = -\frac{\cos\theta}{\Omega G(\theta)} \ln(A[p_k(\theta)]) \quad \text{(A2)}$$

where $A\left[p_k(\theta)\right]$ is the arithmetic mean of $p_k(\theta)$ within a coarse resolution pixel. Based on the semiempirical transfer function, LAI_{exa} is:

$$LAI_{exa} = -\frac{1}{K_{LAI}} \ln\left(G\left[p\left(\rho_{NIR}^k, \rho_R^k\right)\right]\right) \tag{A3}$$

where K_{LAI} is the extinction coefficient, $p\left(\rho_{NIR}^k, \rho_R^k\right)$ represents the kth directional gap probability at fine spatial resolution, which is estimated by Equation (9) in the body of the article. $G\left[p\left(\rho_{NIR}^k, \rho_R^k\right)\right]$ is the geometric mean of $p\left(\rho_{NIR}^k, \rho_R^k\right)$ within a coarse spatial resolution. The approximate LAI is:

$$LAI_{app} = -\frac{1}{K_{LAI}} \ln\left(p\left(A\left[\rho_{NIR}^k\right], A\left[\rho_R^k\right]\right)\right) \tag{A4}$$

where $A\left[\rho_{NIR}^k\right]$ and $A\left[\rho_R^k\right]$ are the arithmetic means of red reflectance ρ_R^k and near-infrared reflectance ρ_{NIR}^k within a coarse resolution pixel, respectively. $p(A[\rho_{NIR}], A[\rho_R])$ is the directional gap probability of that coarse-resolution pixel.

Appendix B

When the scaling bias of LAI is calculated using the TSEM algorithm, an approximate value directly obtains as follows:

$$bias_{TSEM} \approx -\frac{1}{2} f''(x_A) \sum_{k=1}^{N} \frac{(x_k - x_A)^2}{N} = -\frac{1}{2} \mu_{TSEM} Var(X)_{TSEM} \tag{A5}$$

where N is the quantity of subpixels within a coarse resolution pixel, x_A is the arithmetic mean of the input variable $X = \{x_1, x_2, \ldots, x_N\}$, and $f''(x_A)$ is the second derivative at x_A, which is denoted by μ_{TSEM}. x_k is the kth input variable in a coarse pixel. $Var(X)_{TSEM}$ is the variance of X.

References

1. Baret, F.; Weiss, M.; Lacaze, R.; Camacho, F.; Makhmara, H.; Pacholcyzk, P.; Smets, B. GEOV1: LAI and FAPAR essential climate variables and FCOVER global time series capitalizing over existing products. Part1: Principles of development and production. *Remote Sens. Environ.* **2013**, *137*, 299–309. [CrossRef]
2. Wang, J.; Sun, R.; Zhang, H.; Xiao, Z.; Zhu, A.; Wang, M.; Yu, T.; Xiang, K. New Global MuSyQ GPP/NPP Remote Sensing Products From 1981 to 2018. *IEEE J. Sel. Top. Appl. Earth Observ. Remote Sens.* **2021**, *14*, 5596–5612. [CrossRef]
3. Chen, Z.; Jia, K.; Wei, X.; Liu, Y.; Zhan, Y.; Xia, M.; Yao, Y.; Zhang, X. Improving leaf area index estimation accuracy of wheat by involving leaf chlorophyll content information. *Comput. Electron. Agric.* **2022**, *196*, 106902. [CrossRef]
4. Cortés, J.; Mahecha, M.D.; Reichstein, M.; Myneni, R.B.; Chen, C.; Brenning, A. Where Are Global Vegetation Greening and Browning Trends Significant? *Geophys. Res. Lett.* **2021**, *48*, e2020GL091496. [CrossRef]
5. Chen, C.; Park, T.; Wang, X.H.; Piao, S.L.; Xu, B.D.; Chaturvedi, R.K.; Fuchs, R.; Brovkin, V.; Ciais, P.; Fensholt, R.; et al. China and India lead in greening of the world through land-use management. *Nat. Sustain.* **2019**, *2*, 122–129. [CrossRef]
6. Yu, T.; Zhang, Q.; Sun, R. Comparison of Machine Learning Methods to Up-Scale Gross Primary Production. *Remote Sens.* **2021**, *13*, 2448. [CrossRef]
7. Chen, J.M.; Ju, W.M.; Ciais, P.; Viovy, N.; Liu, R.G.; Liu, Y.; Lu, X.H. Vegetation structural change since 1981 significantly enhanced the terrestrial carbon sink. *Nat. Commun.* **2019**, *10*, 4259. [CrossRef]
8. Garrigues, S.; Allard, D.; Baret, F.; Weiss, M. Influence of the spatial heterogeneity on the non-linear estimation of Leaf Area Index from moderate resolution remote sensing data. *Remote Sens. Environ.* **2006**, *105*, 286–298. [CrossRef]
9. Liu, W.H.; Shi, J.C.; Liang, S.L.; Zhou, S.G.; Cheng, J. Simultaneous retrieval of land surface temperature and emissivity from the FengYun-4A advanced geosynchronous radiation imager. *Int. J. Digit. Earth* **2022**, *15*, 198–225. [CrossRef]
10. Wu, H.; Li, Z.-L. Scale Issues in Remote Sensing: A Review on Analysis, Processing and Modeling. *Sensors* **2009**, *9*, 1768–1793. [CrossRef]
11. Zhang, J.; Wang, J.; Sun, R.; Zhou, H.; Zhang, H. A Model-Downscaling Method for Fine-Resolution LAI Estimation. *Remote Sens.* **2020**, *12*, 4147. [CrossRef]

12. Deng, F.; Chen, J.M.; Plummer, S.; Chen, M.; Pisek, J. Algorithm for global leaf area index retrieval using satellite imagery. *IEEE Trans. Geosci. Remote Sens.* **2006**, *44*, 2219–2229. [CrossRef]
13. Liang, S. Numerical experiments on the spatial scaling of land surface albedo and leaf area index. *Remote Sens. Rev.* **2000**, *19*, 225–242. [CrossRef]
14. Tao, X.; Yan, B.; Wang, K.; Wu, D.; Fan, W.; Xu, X.; Liang, S. Scale transformation of Leaf Area Index product retrieved from multiresolution remotely sensed data: Analysis and case studies. *Int. J. Remote Sens.* **2009**, *30*, 5383–5395. [CrossRef]
15. Yin, G.F.; Li, J.; Liu, Q.H.; Li, L.H.; Zeng, Y.L.; Xu, B.D.; Yang, L.; Zhao, J. Improving Leaf Area Index Retrieval Over Heterogeneous Surface by Integrating Textural and Contextual Information: A Case Study in the Heihe River Basin. *IEEE Geosci. Remote Sens. Lett.* **2015**, *12*, 359–363. [CrossRef]
16. Xu, B.D.; Li, J.; Park, T.J.; Liu, Q.H.; Zeng, Y.L.; Yin, G.F.; Yan, K.; Chen, C.; Zhao, J.; Fan, W.L.; et al. Improving leaf area index retrieval over heterogeneous surface mixed with water. *Remote Sens. Environ.* **2020**, *240*, 111700. [CrossRef]
17. Fang, H.; Baret, F.; Plummer, S.; Schaepman-Strub, G. An Overview of Global Leaf Area Index (LAI): Methods, Products, Validation, and Applications. *Rev. Geophys.* **2019**, *57*, 739–799. [CrossRef]
18. Fisher, R.A.; Koven, C.D. Perspectives on the Future of Land Surface Models and the Challenges of Representing Complex Terrestrial Systems. *J. Adv. Model. Earth Syst.* **2020**, *12*, e2018MS001453. [CrossRef]
19. Zhao, W.; Fan, W. Quantitative Representation of Spatial Heterogeneity in the LAI Scaling Transfer Process. *IEEE Access* **2021**, *9*, 83851–83862. [CrossRef]
20. Jin, Z.; Tian, Q.; Chen, J.M.; Chen, M. Spatial scaling between leaf area index maps of different resolutions. *J. Environ. Manag.* **2007**, *85*, 628–637. [CrossRef]
21. Raffy, M. Change of scale in models of remote sensing: A general method for spatialization of models. *Remote Sens. Environ.* **1992**, *40*, 101–112. [CrossRef]
22. Hu, Z.; Islam, S. A framework for analyzing and designing scale invariant remote sensing algorithms. *IEEE Trans. Geosci. Remote. Sens.* **1997**, *35*, 747–755. [CrossRef]
23. Jiang, J.; Liu, X.; Liu, C.; Wu, L.; Xia, X.; Liu, M.; Du, Z. Analyzing the Spatial Scaling Bias of Rice Leaf Area Index From Hyperspectral Data Using Wavelet-Fractal Technique. *IEEE J. Sel. Top. Appl. Earth Observ. Remote Sens.* **2015**, *8*, 3068–3080. [CrossRef]
24. Wu, L.; Liu, X.; Qin, Q.; Zhao, B.; Ma, Y.; Liu, M.; Jiang, T. Scaling Correction of Remotely Sensed Leaf Area Index for Farmland Landscape Pattern With Multitype Spatial Heterogeneities Using Fractal Dimension and Contextural Parameters. *IEEE J. Sel. Top. Appl. Earth Observ. Remote Sens.* **2018**, *11*, 1472–1481. [CrossRef]
25. Wu, L.; Qin, Q.; Liu, X.; Ren, H.; Wang, J.; Zheng, X.; Ye, X.; Sun, Y. Spatial Up-Scaling Correction for Leaf Area Index Based on the Fractal Theory. *Remote Sens.* **2016**, *8*, 197. [CrossRef]
26. Chen, H.; Wu, H.; Li, Z.-L.; Tu, J. An Improved Computational Geometry Method for Obtaining Accurate Remotely Sensed Products via Convex Hulls With Dynamic Weights: A Case Study With Leaf Area Index. *IEEE J. Sel. Top. Appl. Earth Observ. Remote Sens.* **2019**, *12*, 2308–2319. [CrossRef]
27. Wang, J.P.; Wu, X.D.; Wen, J.G.; Xiao, Q.; Gong, B.C.; Ma, D.J.; Cui, Y.R.; Lin, X.W.; Bao, Y.F. Upscaling in Situ Site-Based Albedo Using Machine Learning Models: Main Controlling Factors on Results. *IEEE Trans. Geosci. Remote Sens.* **2022**, *60*, 3095153. [CrossRef]
28. Wu, X.D.; Wen, J.G.; Tang, R.Q.; Wang, J.P.; Zeng, Q.C.; Li, Z.; You, D.Q.; Lin, X.W.; Gong, B.C.; Xiao, Q. Quantification of the uncertainty in multiscale validation of coarse-resolution satellite albedo products: A study based on airborne CASI data. *Remote Sens. Environ.* **2023**, *287*, 113465. [CrossRef]
29. Chen, Y.G. Fractal Modeling and Fractal Dimension Description of Urban Morphology. *Entropy* **2020**, *22*, 961. [CrossRef]
30. Jiang, J.; Ji, X.; Yao, X.; Tian, Y.; Zhu, Y.; Cao, W.; Cheng, T. Evaluation of Three Techniques for Correcting the Spatial Scaling Bias of Leaf Area Index. *Remote Sens.* **2018**, *10*, 221. [CrossRef]
31. Becker, R. The Variance Drain and Jensen's Inequality. *CAEPR Work. Pap.* **2012**, 2004–2012. [CrossRef]
32. Li, W.; Mu, X. Using fractal dimension to correct clumping effect in leaf area index measurement by digital cover photography. *Agric. For. Meteorol.* **2021**, *311*, 108695. [CrossRef]
33. Shi, Y.; Wang, J.; Wang, J.; Qu, Y. A Prior Knowledge-Based Method to Derivate High-Resolution Leaf Area Index Maps with Limited Field Measurements. *Remote Sens.* **2017**, *9*, 13. [CrossRef]
34. Zhang, X.; Yan, G.; Li, Q.; Li, Z.-L.; Wan, H.; Guo, L. Evaluating the fraction of vegetation cover based on NDVI spatial scale correction model. *Int. J. Remote Sens.* **2006**, *27*, 5359–5372. [CrossRef]
35. Qi, J.; Xie, D.; Yin, T.; Yan, G.; Gastellu-Etchegorry, J.; Li, L.; Zhang, W.; Mu, X.; Norford, L. LESS: LargE-Scale remote sensing data and image simulation framework over heterogeneous 3D scenes. *Remote Sens. Environ.* **2019**, *221*, 695–706. [CrossRef]
36. Xu, Y.; Xie, D.; Qi, J.; Yan, G.; Mu, X.; Zhang, W. Influence of woody elements on nadir reflectance of forest canopy based on simulations by using the LESS model. *J. Remote Sens.* **2021**, *25*, 1138–1151.
37. Nilson, T. A theoretical analysis of frequency of gaps in plant stands. *Agric. Meteorol.* **1971**, *8*, 25. [CrossRef]
38. Wang, W.-M.; Li, Z.-L.; Su, H.-B. Comparison of leaf angle distribution functions: Effects on extinction coefficient and fraction of sunlit foliage. *Agric. For. Meteorol.* **2007**, *143*, 106–122. [CrossRef]
39. Yan, G.; Hu, R.; Luo, J.; Weiss, M.; Jiang, H.; Mu, X.; Xie, D.; Zhang, W. Review of indirect optical measurements of leaf area index: Recent advances, challenges, and perspectives. *Agric. For. Meteorol.* **2019**, *265*, 390–411. [CrossRef]

40. Xiao, Z.; Liang, S.; Wang, J.; Chen, P.; Yin, X.; Zhang, L.; Song, J. Use of General Regression Neural Networks for Generating the GLASS Leaf Area Index Product From Time-Series MODIS Surface Reflectance. *IEEE Trans. Geosci. Remote Sens.* **2014**, *52*, 209–223. [CrossRef]
41. Fang, H. Canopy clumping index (CI): A review of methods, characteristics, and applications. *Agric. For. Meteorol.* **2021**, *303*, 18. [CrossRef]
42. Ryu, Y.; Nilson, T.; Kobayashi, H.; Sonnentag, O.; Law, B.E.; Baldocchi, D.D. On the correct estimation of effective leaf area index: Does it reveal information on clumping effects? *Agric. For. Meteorol.* **2010**, *150*, 463–472. [CrossRef]
43. Tang, S.; Chen, J.; Zhu, Q.; Li, X.; Chen, M.; Sun, R.; Zhou, Y.; Deng, F.; Xie, D. LAI inversion algorithm based on directional reflectance kernels. *J. Environ. Manag.* **2007**, *85*, 638–648. [CrossRef]
44. Baret, F.; Guyot, G. Potentials and limits of vegetation indices for LAI and APAR assessment. *Remote Sens. Environ.* **1991**, *35*, 161–173. [CrossRef]
45. Chen, J.M.; Menges, C.H.; Leblanc, S.G. Global mapping of foliage clumping index using multi-angular satellite data. *Remote Sens. Environ.* **2005**, *97*, 447–457. [CrossRef]
46. Ma, L.; Li, C.; Tang, B.; Tang, L.; Bi, Y.; Zhou, B.; Li, Z.-L. Impact of spatial LAI heterogeneity on estimate of directional gap fraction from SPOT-satellite data. *Sensors* **2008**, *8*, 3767–3779. [CrossRef]